ACS Photonics

Letter

pubs.acs.org/journal/apchd5

Fast Room-Temperature Detection of Terahertz Quantum Cascade Lasers with Graphene-Loaded Bow-Tie Plasmonic Antenna Arrays

Riccardo Degl'Innocenti,*[,†] Long Xiao,[†,‡] David S. Jessop,[†] Stephen J. Kindness,[†] Yuan Ren,[†] Hungyen Lin,[§,∥] J. Axel Zeitler,[§] Jack A. Alexander-Webber,[‡] Hannah J. Joyce,[‡] Philipp Braeuninger-Weimer,[‡] Stephan Hofmann,[‡] Harvey E. Beere,[†] and David A. Ritchie[†]

[†]Cavendish Laboratory, University of Cambridge, J. J. Thomson Avenue, Cambridge CB3 0HE, United Kingdom

[‡]Department of Engineering, University of Cambridge, J. J. Thomson Avenue, Cambridge CB3 0FA, United Kingdom

[§]Department of Chemical Engineering and Biotechnology, University of Cambridge, Pembroke Street, Cambridge CB2 3RA, United Kingdom

[∥]Department of Engineering, Lancaster University, Lancaster LA1 4YW, United Kingdom

S *Supporting Information*

ABSTRACT: We present a fast room-temperature terahertz detector based on interdigitated bow-tie antennas contacting graphene. Highly efficient photodetection was achieved by using two metals with different work functions as the arms of a bow-tie antenna contacting graphene. Arrays of the bow-ties were fabricated in order to enhance the responsivity and coupling of the incoming light to the detector, realizing an efficient imaging system. The device has been characterized and tested with a terahertz quantum cascade laser emitting in single frequency around 2 THz, yielding a responsivity of ∼34 μA/W and a noise-equivalent power of ∼1.5 × 10^{-7} W/$Hz^{1/2}$.

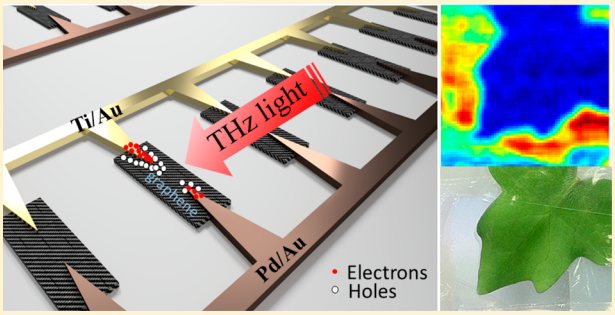

KEYWORDS: *graphene, photodetection, terahertz, quantum cascade laser, optical modulator*

Terahertz (THz) photonics is attracting an increasing level of attention in the scientific community and represents a rapidly growing research area because of several unique applications in spectroscopy, sensing, communications, and imaging. Owing to the unique characteristics of this frequency range, such as its nonionizing nature and its extreme sensitivity to tissue water content, THz imaging holds great promise for diagnostics and nondestructive analysis of biological tissues. Detection of THz radiation without using coherent approaches, e.g., broadband time-domain spectroscopic systems, remains particularly elusive and has traditionally relied on intrinsically slow (<100 Hz) detectors such as pyroelectric detectors or Golay cells. Recently, graphene and other bidimensional nanomaterials have been investigated as viable detection materials in a few review[1−3] and research articles.[4−11] Graphene-based THz detectors operate via several distinct physical mechanisms; the most common are the photovoltaic, bolometric, and photothermal effect.[1,2] However, even though graphene detection is intrinsically fast, the responsivity is low, making the detection of THz radiation particularly difficult. A few attempts have been explored to produce more efficient devices and boost the photodetectors' responsivity. Among these, a noteworthy approach consisted of integrating graphene with a silicon-heterostructure waveguide in a frequency range spanning from the near- to the mid-infrared range.[4] An alternative approach is based on the exploitation of plasmonics, thus increasing the light concentration and interaction with graphene.[6,7] Finally, field-effect transistors implementing either graphene,[8] topological insulators,[9] or black-phosphorus[10] have demonstrated photodetection at 0.3 THz at room temperature. However, all these architectures are based on exfoliated rather than large-area (>mm^2) chemical vapor deposited (CVD) material, which requires the implementation of antennas in order to efficiently focus the light to the device active area. A high-efficiency detector operating at room temperature and using broadband THz pulses has been reported operating on the photothermoelectric effect.[11] It should also be mentioned a parallel line of research based on nanowires as detecting elements.[12] The main hurdle of the implementation of these highly efficient elements in complex architecture resides mainly in their inherent fabrication difficulty and/or in the alignment of multiple elements, even though significant progress has been reported recently.[13] It is worth highlighting that even though a number of articles claim to report THz detectors, only a few have been demonstrated with a THz source emitting above 1 THz, and none with a THz quantum cascade laser (QCL), to the best of our knowledge.

Received: June 16, 2016
Published: September 20, 2016

DOI: 10.1021/acsphotonics.6b00405
ACS Photonics 2016, 3, 1747−1753

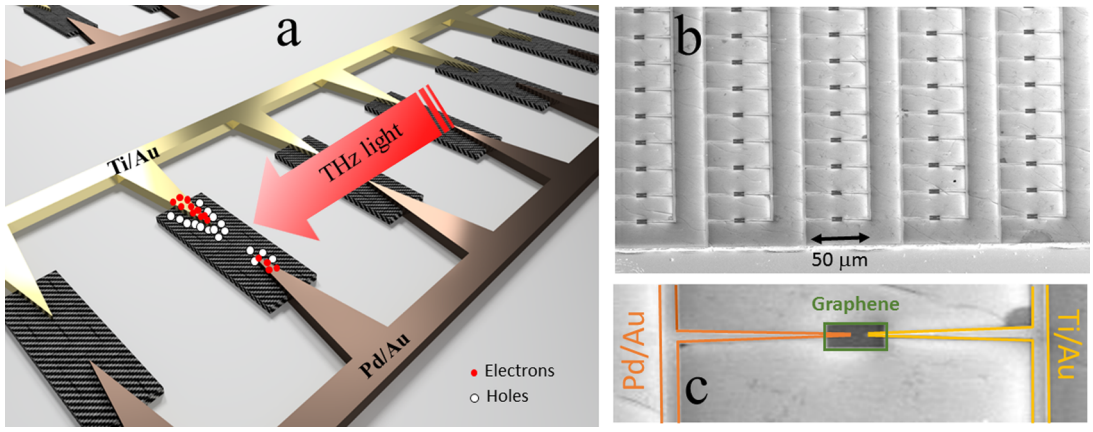

Figure 1. (a) Basic principle of the bow-tie array detector: the incoming resonant THz light translates into a charge unbalancing between the two asymmetric antenna's arms, summing up to a detectable coherent photocurrent. (b) Scanning electron microscope image of an array and a detailed image (c) of a single element. The graphene area contacted by the two different metal antenna's arms is clearly distinguishable.

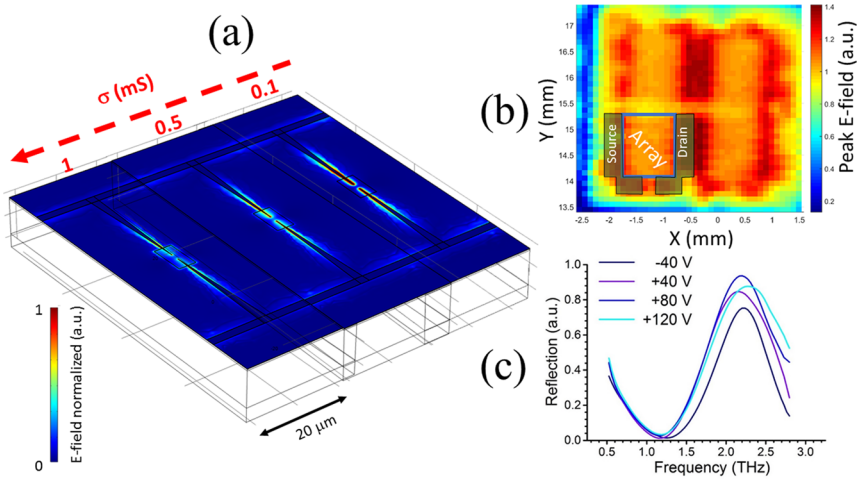

Figure 2. (a) Simulation reproducing the bow-tie unit of the array implemented in these measurements performed with Comsol Multiphysics of the normalized E-field at the resonant frequency of 1.9 THz for different values of the graphene conductivity. The corresponding reflectivity measurements at different frequencies are reported in the SI. (b) THz reflectivity map of the sample corresponding to a gate voltage of 120 V obtained with a time-domain spectroscopic system from Teraview. The four arrays and the metallic contacts are clearly distinguishable by observing the peak of the E-field. Each pixel corresponds to a waveform in the time domain that, after having being truncated, Fourier-transformed, and normalized yields the plasmonic resonances shown in (c). These resonances are referred to the bottom left array in (b) for different gate voltages with respect to the grounded source/drain contacts.

RESULTS AND DISCUSSION

Here we demonstrate an efficient room-temperature THz detector based on interdigitated bow-tie antennas asymmetrically doping monolayer graphene, to exploit the photovoltaic effect, although it cannot be excluded a contribution due to the photothermoelectric effect. In the photovoltaic effect the built-in electric field at a metal−graphene junction separates the photoexcited electron−hole pairs. Metals with different work function provide different doping in the contact area.[1,2] One arm of each bow-tie antenna was fabricated using Ti to achieve n-type doping in the adjacent graphene, whereas the other arm was fabricated using Pd to achieve p-type doping. This asymmetric doping creates an electric field profile across the device, as previously described for graphene-based photodetectors operating at optical communications frequencies.[5] The detector was integrated in an imaging system and tested with a single-metal bound-to-continuum QCL single frequency emitting at 2.005 THz. A similar approach has been reported by implementing metallic gratings integrated in a logarithmic antenna for the focusing of the THz pulses emitted by a free-electron laser[14] to a graphene flake. The reported responsivity was of a few nA/W, and the physical detection mechanism was attributed to a photoinduced bolometric effect. Because of the efficient photocurrent buildup achieved by the multiple elements in the array and the boosting of the light−matter interaction due to the plasmonic resonance, we achieved a record responsivity of ∼34 μA/W, which allows the implementation of THz QCL sources with typical incident powers of a few mW. In the photovoltaic effect photogenerated electron−hole pairs are separated at the junction by an internal electric field that arises due to the asymmetric doping profile across the graphene. This can lead to an efficient buildup of photocurrent. The photothermoelectric effect is an alternative mechanism of operation that, in contrast, is due to the hot carriers[15] photogenerated in graphene, which for two differently doped graphene regions leads to a photovoltage via the Seebeck effect. In both scenarios the net effect is a charge asymmetry on the two arms of the resonant antenna element when the THz

DOI: 10.1021/acsphotonics.6b00405
ACS Photonics 2016, 3, 1747−1753

radiation is impinging onto the detector, as shown in the schematic of Figure 1a. Scanning electron microscopy (SEM) images of the fabricated devices are presented in Figure 2b and c; the graphene array shunting each bow-tie element is clearly visible. The device has been fabricated from CVD-grown monolayer graphene transferred on top of a SiO_2/Si substrate. A few steps of optical/electron beam lithography and thermal/e-beam evaporations, as detailed in the Methods section, were required in order to produce the final device. The sample was then mounted on a Au-ceramic chip carrier and wire-bonded to allow electrical testing. The sample consists of four independent arrays, each centered at a different resonant frequency. The array used in all the photodetection measurements consists of 615 bow-tie antennas distributed over a 1.2 mm^2 area. The total length of the unit cell was scaled in order to achieve a broad lithographic tuning around 2 THz. This spectral region is covered both by single-frequency emitting THz QCLs and by THz time domain spectroscopic systems. The main resonances of such an antenna element arrangement are taking place when the major axis length of the single arm is $\sim m\lambda_s/2$, where m is an odd number and λ_s is the wavelength of the surface plasmon supported by the metallic feature over the substrate. The surface plasmon wavelength λ_s is proportional to $\lambda_0\sqrt{\frac{(\varepsilon_{sub}+\varepsilon_{m1,2})}{\varepsilon_{sub}\varepsilon_{m1,2}}}$ with λ_0 being the vacuum wavelength and ε_{sub}, ε_m the real part of the dielectric constant of the substrate and of the metal, respectively. Since the absolute values of the dielectric constant for the two metals Pd and Ti ($|\varepsilon_{m1}|$, $|\varepsilon_{m2}|$) are considerably higher than the dielectric constant of the substrate ($|\varepsilon_{sub}|$), the design of a bow-tie antenna whose arms are fabricated with two different metals has a minor effect on the resonant frequency compared to a conventional single-metal antenna. It does however increase the damping of the resonances since the imaginary part of the dielectric constant of Pd/Ti is larger than in Au. Finite element simulations, shown in Figure 2a, have been performed with the commercial software Comsol Multiphysics v 5.1 in order to investigate and calibrate the plasmonic resonances around 2 THz. The simulation window is based on a single unit cell with periodic boundary conditions. A Drude model was implemented to simulate the optical properties of Pd/Ti/Au[16] and graphene[17,18] through the complex permittivity. The reflectivity of an incident plane wave having polarization along the major axis of the bow-tie is monitored through the $|S_{11}|^2$ parameter. Figure 2a shows the normalized electric field for the bow-tie antennas yielding a resonant frequency around 1.9 THz for different values of the graphene conductivity σ between 0.1 and 1 mS, which is commensurate with CVD-grown graphene that has been processed as reported in refs 19−21. The tapering of the arms focuses the THz radiation onto the graphene region. By changing the graphene conductivity via the back gate the damping of these resonances is dynamically modified. In fact, this device can be operated also as an ultrafast amplitude modulator, as described in more detail elsewhere.[19] Figure 2b shows the THz reflectivity map of the device, obtained by using a commercial THz time domain spectroscopy (THz-TDS) system (TPI Imaga 2000, TeraView, UK), based on photoconductive antennas and operating in reflection mode.[20,21] From the peak electric field reflected, as shown in Figure 2b it is possible to clearly distinguish the different areas on the device, such as the source and drain metallic pads and the four different arrays. We focused our attention on the bottom left panel, since it has the best frequency match with a THz QC laser emitting in single frequency around 2 THz. A set of measurements similar to what is reported in Figure 2b has been acquired for different gate voltages with respect to the grounded source/drain pads. By using a similar procedure already reported in refs 19 and 20 it was possible to extract the frequency response of this array for different gate voltages. The resonant frequency is measured around 2.1 THz, blue-shifted by ∼200 GHz with respect to the simulations reported in the Supporting Information (SI). The modulation depth measured and reported in Figure 2c is ∼21%, in fair agreement with the 28% simulated modulation depth corresponding to a change in graphene conductivity between 0.1 and 1 mS. The maximum of the reflectivity peak achieved in Figure 2c is consistent with the maximum value of the source/drain resistance and the minimum graphene conductivity. However, these are representative values since a more detailed gate voltage scan could increase the measured modulation depth and the simulated values refer to a similar, but not identical, sample. The electrical characterization of the sample is shown and commented in more detail in the SI. The resistance between source and drain, R_{SD}, was recorded at different gate biases in order to find the minimum conductivity point, which cannot be identified conclusively as the Dirac point because of the complex device architecture and the contributions of the metallic pads. While the source/drain resistance shows consistent values over months of measurements, the maximum resistance, R_{SD}^{Max}, position has shifted from the initial ∼90 V to ∼110 V, which are compatible with exposed p-doped CVD-grown graphene. These values are also consistent with the THz-TDS measurements reported in Figure 2c. Baking the sample at a temperature above 150 °C for a few hours helped in bringing the R_{SD}^{Max} back to the pristine value temporally. This shift in the Dirac point is due to the choice of leaving the graphene exposed, therefore more susceptible to atmospheric adsorbants.[22] This effect can be reduced by passivation with a top dielectric. However, the graphene was left exposed in order to have a mobility as high as possible since the implementation with standard methods, e.g., thermal evaporation, of a dielectric layer has been reported to reduce the mobility[23] and consequently the photocurrent.

The detector was then implemented in an imaging system, schematically shown in Figure 3, implementing QCLs as THz sources for photocurrent characterization and imaging. The laser is a single plasmon device fabricated from a bound-to-continuum design,[24] emitting around 2 THz in single frequency around maximum output power. The QCL was operated in pulsed mode with a repetition rate of 10 kHz and 30% duty cycle at 5 K. The THz radiation was collimated by a 2 in. effective focal length parabolic mirror (PB). Two more PB mirrors focused the THz light to the object of interest, e.g., a leaf, and collimated the transmitted radiation. A final 1 in. PB mirror focused the light to the detector area. A 1 mm diameter pinhole was placed as close as possible to the detector in order to ensure that the illuminated area was within the detector area. A double-side polished Si wafer, not shown in Figure 3, was implemented as a beam splitter in order to monitor the THz radiation reflected from the array and extrapolate the responsivity. The QCL was operated in continuous pulse mode when imaging and in low-frequency gate mode when detecting the reflected power. In order to finely align the position of the device to the incoming THz beam, it was operated and configured as an amplitude modulator following a procedure previously reported.[20] By maximizing the modulated

DOI: 10.1021/acsphotonics.6b00405
ACS Photonics 2016, 3, 1747−1753

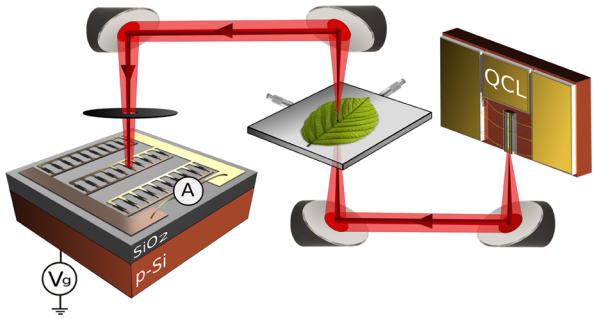

Figure 3. Schematic of the setup used for the photodetection and imaging of large-size objects. The THz light emitted from a QCL is collimated by a 2 in. focal length parabolic mirror. Two other similar mirrors focus the radiation to the imaging plane and then collimate the transmitted light to a final 1 in. focal length parabolic mirror. A 1 mm diameter aperture placed as close as possible to the detector ensured that the illuminated area was not larger than the array area. A lock-in amplifier, having the reference as the repetition rate of the QCL, is placed in series between the source and drain contacts in order to measure the photocurrent. Finally, by changing the bias of the gate with respect to source and drain contacts with a Keithley voltage/current generator, it was possible to set the working point.

amplitude signal, we ensured that the illumination area, defined by a 1 mm pinhole diameter, was centered on the detector. The electrical configuration used for photodetection implemented a lock-in amplifier placed in series with the source and drain pads. One Keithley model 2400 source/measure unit was used to change the voltage of the gate with respect to the source/drain contacts, thus setting the working point. A constant bias of a few mV with both polarities was then applied between source and drain while the current passing through was monitored by the lock-in amplifier (Signal Recovery, model 7265). The reference signal on the lock-in amplifier was the 10 kHz applied to the QCL. A demodulated signal that increased as the gate voltage applied approached the Dirac point appeared when the THz radiation emitted by the QCL was polarized along the main axis of the antennas and impinged onto the detector, as shown in Figure 4a. Conversely, the same measurements performed when blocking the THz radiation did not yield any signal emerging from the noise floor by changing the gate voltage. A maximum photocurrent of ∼430 pA was measured at 95 V gate bias for an estimated incident THz peak power of ∼0.8 mW. This corresponds to a responsivity of ∼0.5 μA/W considering the total power impinging onto the detector. This value of the responsivity has been calculated assuming the whole area of the device is illuminated by the irradiation. If, instead, the effective power is scaled considering the graphene areas, then the responsivity is ∼34 μA/W.

The system at the Dirac point behaves as a p−n−n^+ junction, corresponding to the Pd−graphene−Ti contacts.[25−27] This trend is well represented by the measurements acquired without a pinhole in order to maximize the signal and is shown in Figure 4b. When the system is forward biased, the photocurrent is as high as 0.85 nA at the Dirac point. At reverse biasing a similar trend was observed but with lower efficiency. Further negative bias of the device led to negligible photocurrent. A zero bias between source and drain yielded a comparable photocurrent to forward bias, but a significantly higher noise level. A further set of measurements, reported in the SI, was taken with the polarization of the incident radiation perpendicular to the antennas' main axis. In this experimental configuration we are not expecting any resonant effect arising from the plasmonic bow-tie antenna. Accordingly, no detectable photocurrent was measured and the signal acquired at different gate voltages was always within the noise floor. Noise equivalent power (NEP) measurements were acquired for completeness and are reported in the SI, yielding a minimum value of the noise of ∼1.5 × 10^{-7} W/$Hz^{1/2}$. It is worth mentioning that the measurements shown in Figure 4 and the ones reported in the SI were acquired in a time frame of a few months, after having completely realigned the system each time. The maximal photocurrent signal in Figure 4a is maximal around 95 V, consistent with the THz-TDS measurements presented in Figure 2c and the electrical characterization reported in the SI.

In order to get further insight into the physics of the photodetection mechanism and to investigate the main physical mechanisms underlying the detection process, a simplified model has been implemented. The photovoltaic (PV) effect arises in our experimental arrangement from the imbalance between the photogenerated electron−hole pairs separated at the two metal−graphene junctions constituted by the antenna

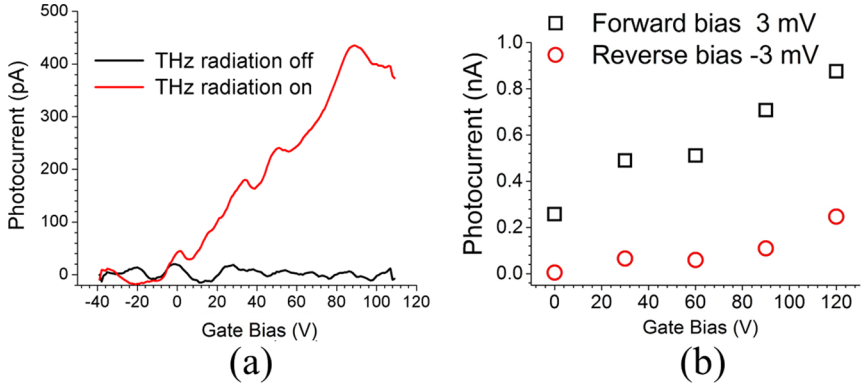

Figure 4. (a) Photocurrent measurements as a function of the gate voltage. When the THz beam emitted from the QCL is impinging onto the photodetector, a signal emerges from the noise, reaching the maximal value at the Dirac point around 95 V. Conversely, when the radiation is blocked, no detectable signal is observed. The QCL was biased at maximum output power in continuous pulse mode with a repetition rate of 10 kHz, 30% duty cycle, and 5 K operating temperature. The detector was forward biased with 1 mV between source and drain. (b) Similar measurements were acquired by removing the pinhole and show a significant asymmetry in the photocurrent depending on the biasing. It is worth repeating that this set of measurements was acquired a few months after the first set, shown in (a), and that a shift in the Dirac point was observed.

DOI: 10.1021/acsphotonics.6b00405
ACS Photonics 2016, 3, 1747−1753

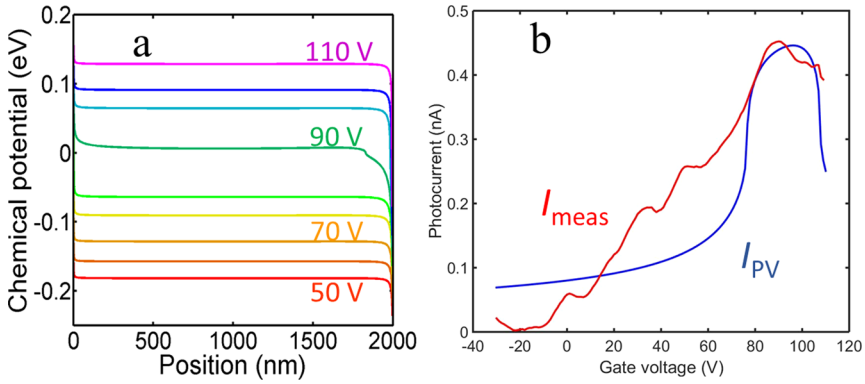

Figure 5. (a) Chemical potential across the Ti−graphene−Pd junction for different gate voltages from the Dirac point V_D. The band bending suggests an n-doping and p-doping across the graphene region more evident at the Dirac point. (b) Calculated photovoltaic current, I_{PV}, blue trace, and measured photocurrent, I_{meas}, red trace, at different gate voltages: the two traces are in good agreement.

arms. The asymmetric doping of the two metallic elements of the bow-tie antenna contacting graphene realizes a n^+-n-p junction, corresponding to the Ti arm, graphene region, and Pd arm, respectively. This effect is clearly shown in Figure 5a, where the chemical potential at different gate voltages with respect to the Dirac point has been calculated along the graphene region contacting the two metallic arms. In principle, the photothermoelectric effect (PT) could also contribute to the total photocurrent. The PT effect is due to the Seebeck effect at two different doped graphene regions. This mechanism is particularly effective in graphene because of the fast electron temperature rise and slow electron−lattice cooling rates. The PT effect can be identified by multiple changes in the photocurrent direction, as the Fermi energy is varied along the Dirac cone.[15] In none of the photocurrent measurements recorded at different back-gate voltages was a sign reversal observed. The photoinduced bolometric effect, which arises when the incident light modifies either the carriers' mobility or their number, could in principle also contribute to the photocurrent. However, the presented device can operate without the application of a bias between source and drain, in contrast to any bolometric detection scheme, with photocurrent signals as high as in forward bias, but with larger noise level, as shown in the SI. As a consequence, the main photodetection mechanism was attributed to the PV effect. We follow the approach reported in ref 15, as described in more detail in the Methods section. Figure 5b reports the best fit for the PV effect to the experimental data that has been obtained by normalizing the photocurrent shown in Figure 4a and the device resistance characterization reported in the SI. Because of the approximations carried out in the theoretical modeling and the limited experimental data available, we cannot conclusively weight the two contributions. By modifying the carrier concentrations optically instead of using electrostatic gating, it could be possible to determine the time scale for the two detection mechanisms, thus helping to refine the picture. The acquisition of the photodetection signal at different device temperatures would further allow us to investigate contributions to the photocurrent due to the bolometric effect. However, this is beyond the scope of the present paper.

Finally, following a well-consolidated tradition in THz imaging,[28] we performed the imaging of a leaf. Instead of focusing our attention on the definition of the water content in the leaf's veins, we acquired a picture in transmission of the same leaf at different gate voltages, in order to characterize the bias dependence and the limits of the detector. Similar to what is shown in Figure 3, the leaf has been secured in the focus of a *xy* imaging system and the transmitted power has been recorded by the photodetector at different positions of the leaf with respect to the beam focus. The photodetector was forward biased with 7 mV, and the photocurrent detected without the object in the optical path was ∼430 pA at 110 V gate bias. The lock-in amplifier time constant was set to 50 ms, a time scale that is almost prohibitive for standard room detectors such as pyroelectric detectors or Golay cells. The results of the imaging are reported in Figure 6 for the gate held at 0, 80, and 110 V.

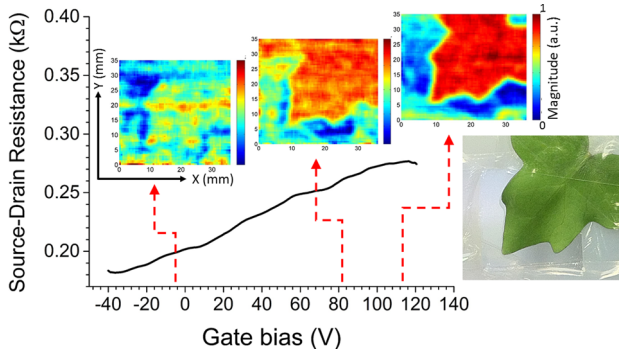

Figure 6. THz imaging of a leaf obtained with the setup shown in Figure 3. The QCL was emitting at 2.005 THz in single-frequency mode and was operated at 5 K temperature, 10 kHz repetition rate, and 30% duty cycle. The photodetector was forward biased at 7 mV. By varying the gate bias of the device the THz picture of the original object, whose optical micrograph picture is also shown for completeness, become sharper. The tip of the leaf in the bottom left corner of the picture is immobilized by using Scotch tape, instead of PVC cling film; this difference is not observed in the visible but is clear in the THz region. The pictures report the magnitude values as read by the lock-in at 0, 80, and 110 V gate bias.

There is a clear correspondence between the image acquired and the optical image of the leaf that becomes more distinguishable above 80 V applied to the gate.

In conclusion, we presented a photodetector operating at room temperature in the THz frequency range based on interdigitated bow-tie antennas shunted by a graphene array. The asymmetrical doping of the graphene area, due to the different metals used to fabricate the antennas' elements, gives rise to a photocurrent that depends also on the average position of the graphene Fermi energy, controlled by a gate voltage. The

DOI: 10.1021/acsphotonics.6b00405
ACS Photonics 2016, 3, 1747−1753

underlying mechanisms of detection, which is mainly attributed to the photovoltaic effect, have been investigated. The device, which can also be operated as an efficient THz amplitude modulator, has been characterized by both a broadband THz-TDS system and a 2 THz QCL reporting a responsivity of 34 μA/W. Although the device operates with remarkable characteristics, there is still plenty of room for optimization. By encapsulating the graphene film with a top dielectric using atomic layer deposition (e.g., Al_2O_3[29]), it is possible to shift the Dirac point to lower values without affecting its mobility and reduce the hysteresis. By acting on the geometry of the system and optimizing the metal thickness and the overlap of the antenna's arms with the graphene, it is possible to further boost the efficiency, improving the plasmonic resonance and the light−matter interaction. The implementation of THz matching layers based on reduced graphene oxide[30] and the replacement of metal contacts with $FeCl_3$-intercalated graphene[31] represent two strategies that can be exploited to increase the graphene absorption. Finally, a wide-bandwidth trans-impedance amplifier would allow the detection of mV instead of nA, which would simplify all the electronics involved in the experimental apparatus. Before proceeding in this direction, an investigation of pick-up noises and interferences with all the other equipment present in the laboratory is required in order to adequately calibrate such an amplifier.

METHODS

Fabrication. Sample fabrication starts with the transfer of monolayer graphene to a SiO_2/Si substrate (300 nm/525 μm thick) grown by chemical vapor deposition.[32,33] The Si substrate was boron-doped (~20 Ω·cm) to allow electrostatic gating of the device. The CVD graphene growth was performed on Cu foils using CH_4 as the precursor and PMMA (poly(methyl methacrylate)) as a support for the transfer followed by $FeCl_3$ chemical etching to remove the Cu. A first step of optical lithography was needed in order to realize the first alignment marks and source and drain contact areas. A first step of electronic beam lithography and oxygen plasma etching was used to realize the arrays of 4 × 8 μm^2 graphene regions covering a total area of 1.2 × 1 mm^2. The two interdigitated arms of the bow-tie arrays were achieved with two steps of double-layer electron beam lithography followed by thermal evaporation of Ti/Au (nominal thickness 60/15 nm) and e-beam evaporation of Pd/Au (nominal thickness 60/15 nm) and lift-off, respectively. The bow-tie elements are separated by a distance of 2 μm. The total length L of the unit cell in the four arrays is 51, 49, 48, and 47 μm. The pitch of the antenna arrays was kept fixed to 1.55L between the rows and to 0.33L between two consecutive elements. The antenna arms' tapering angle was 5°. The sample was then cleaved and mounted on a Au ceramic chip carrier with conductive Ag paste. The final step consisted in wire-bonding the device to allow full electrical characterization and photocurrent measurements.

Photovoltaic and Photothermoelectric Modeling. The photocurrent contribution arising from the photovoltaic effect, I_{PV}, is described in one dimension by the equation[15]

$$I_{PV} = \frac{\eta e n W \int_0^d \sigma^{-1}(y)\, \nabla U(y)\, dy}{\int_0^d \sigma^{-1}(y)\, dy}$$

where y is the distance from the Ti electrode, d is the total length of the graphene between the electrodes, W is the width of the graphene channel between the electrodes, η is the mobility, which was assumed to be 1000 cm^2/V·s, e is the electronic charge, n is the steady-state density of photoexcited carriers, $\sigma(y)$ is the electrical conductivity, and $U(y)$ is the electric field profile. The electric field profile and electrical conductivity were calculated based on the position-dependent chemical potential of the graphene in contact with the two metals of the bow-tie, as described in ref 26. Assuming a photoabsorption of 2.34% and an internal quantum efficiency of 7%,[34] the curve that best reproduces the experimental data, shown in Figure 5b, is obtained with a fixed channel width of 200 mm, in good agreement with the values reported for the region where the built-in field separates the photoexcited carriers in metal−graphene junction.[35]

ASSOCIATED CONTENT

Supporting Information

The Supporting Information is available free of charge on the ACS Publications website at DOI: 10.1021/acsphotonics.6b00405.

Electrical characterization of the sample; simulation performed with the finite element commercial software Comsol Multiphysics; simulated terahertz reflection response of the device arrays and their frequency/amplitude response at different conductivity levels of the graphene film; photocurrent acquired at different gate voltages with and without the THz light impinging on the sample; comparison between the photocurrent measured with the THz light impinging on the sample with the polarization parallel and perpendicular to the main axis of the plasmonic antennas; measured noise-equivalent power of the photodetector at different biasing conditions (PDF)

AUTHOR INFORMATION

Corresponding Author

*E-mail (R. Degl'Innocenti): rd448@cam.ac.uk.

Notes

The authors declare no competing financial interest.

Additional data sets related to this publication are available from the Cambridge University data repository at http://dx.doi.org/10.17863/CAM.4505.

ACKNOWLEDGMENTS

R.D., Y.R., and H.E.B. acknowledge financial support from the Engineering and Physical Sciences Research Council (Grant No. EP/J017671/1, Coherent Terahertz Systems). S.H. acknowledges funding from EPSRC (Grant No. EP/K016636/1, GRAPHTED). H.L. and J.A.Z. acknowledge financial support from the EPSRC (Grant No. EP/L019922/1). J.A.A.-W. acknowledges a Research Fellowship from Churchill College, Cambridge. H.J.J. thanks the Royal Commission for the Exhibition of 1851 for her Research Fellowship.

REFERENCES

(1) Koppens, F. H. L.; Mueller, T.; Avouris, P.; Ferrari, A. C.; Vitiello, M. S.; Polini, M. Photodetectors based on graphene, other two-dimensional materials and hybrid systems. *Nat. Nanotechnol.* **2014**, *9*, 780−793.

DOI: 10.1021/acsphotonics.6b00405
ACS Photonics 2016, 3, 1747−1753

(2) Sun, Z.; Chang, H. Graphene and Graphene-like Two-Dimensional Materials in Photodetection: Mechanisms and Methodology. *ACS Nano* **2014**, *8*, 4133−4156.
(3) Withers, F.; Bointon, T. H.; Craciun, M. F.; Russo, S. All-Graphene Photodetectors. *ACS Nano* **2013**, *7*, 5052−5057.
(4) Wang, X.; Cheng, Z.; Xu, K.; Tsang, h. K.; Xu, J. B. High-responsivity graphene/silicon-heterostructure waveguide photodetectors. *Nat. Photonics* **2013**, *7*, 888−891.
(5) Mueller, T.; Xia, F.; Avouris, P. Graphene photodetectors for high-speed optical communications. *Nat. Photonics* **2010**, *4*, 297−301.
(6) Liu, Y.; Cheng, R.; Liao, L.; Zhou, H.; Bai, J.; Liu, G.; Liu, L.; Huang, Y.; Duan, X. Plasmon resonance enhanced multicolour photodetection by graphene. *Nat. Commun.* **2011**, *2*, 579.
(7) Echtermeyer, T. J.; Britnell, L.; Jasnos, P. K.; Lombardo, A.; Gorbachev, R. V.; Grigorenko, A. N.; Geim, A. K.; Ferrari, A. C.; Novoselov, K. S. Strong plasmonic enhancement of photovoltage in graphene. *Nat. Commun.* **2011**, *2*, 458.
(8) Vicarelli, L.; Vitiello, M. S.; Coquillat, D.; Lombardo, A.; Ferrari, A. C.; Knap, W.; Polini, M.; Pellegrini, V.; Tredicucci, A. Graphene field-effect transistors as room-temperature terahertz detectors. *Nat. Mater.* **2012**, *11*, 865−871.
(9) Viti, L.; Coquillat, D.; Politano, A.; Kokh, K. A.; Aliev, Z. S.; Babanly, M. B.; Tereshchenko, O. E.; Knap, W.; Chulkov, E. V.; Vitiello, M. S. Plasma-Wave Terahertz Detection Mediated by Topological Insulators Surface States. *Nano Lett.* **2016**, *16*, 80−87.
(10) Viti, L.; Hu, J.; Coquillat, D.; Politano, A.; Knap, W.; Vitiello, M. S. Efficient Terahertz detection in black-phosphorus nano-transistors with selective and controllable plasma-wave, bolometric and thermoelectric response. *Sci. Rep.* **2016**, *6*, 20474.
(11) Cai, X.; Sushkov, A. B.; Suess, R. J.; Jadidi, M. M.; Jenkins, G. S.; Nyakiti, L. O.; Myers-Ward, R. L.; Li, S.; Yan, J.; Gaskill, D. K.; Murphy, T. E.; Drew, H. D.; Fuhrer, M. S. Sensitive room-temperature terahertz detection via the photothermoelectric effect in graphene. *Nat. Nanotechnol.* **2014**, *9*, 814−819.
(12) Peng, K.; Parkinson, P.; Fu, L.; Gao, Q.; Jiang, N.; Guo, Y.-N.; Wang, F.; Joyce, H. J.; Boland, J. L.; Tan, H. H.; Jagadish, C.; Johnston, M. B. Single Nanowire Photoconductive Terahertz Detectors. *Nano Lett.* **2015**, *15*, 206−210.
(13) Chen, X.; Liu, H.; Li, Q.; Chen, H.; Peng, R.; Chu, S.; Cheng, B. Terahertz detectors arrays based on orderly aligned InN nanowires. *Sci. Rep.* **2015**, *5*, 13199.
(14) Mittendorff, M.; Winner, S.; Kamann, J.; Eroms, J.; Weiss, D.; Schneider, H.; Helm, M. Ultrafast graphene-based broadband THz detector. *Appl. Phys. Lett.* **2013**, *103*, 021113.
(15) Song, J. C. W.; Rudner, M. S.; Marcus, C. M.; Levitov, L. S. Hot Carrier Transport and Photocurrent Response in Graphene. *Nano Lett.* **2011**, *11*, 4688−4692.
(16) Ordal, M. A.; Long, L. L.; Bell, R. J.; Bell, S. E.; Bell, R. R.; Alexander, R. W.; Ward, C. A. Optical properties of the metals Al, Co, Cu, Au, Fe, Pb, Ni, Pd, Pt, Ag, Ti, and W in the infrared and far infrared. *Appl. Opt.* **1983**, *22*, 1099−1119.
(17) Dawlaty, J. M.; Shivaraman, S.; Strait, J.; George, P.; Chandrashekhar, M.; Rana, F.; Spencer, M. G.; Veksler, D.; Chen, Y. Measurement of the optical absorption spectra of epitaxial graphene from terahertz to visible. *Appl. Phys. Lett.* **2008**, *93*, 131905.
(18) Sensale-Rodriguez, B.; Yan, R.; Kelly, M. M.; Fang, T.; Tahy, K.; Hwang, W. S.; Jena, D.; Liu, L.; Xing, H. G. Broadband graphene terahertz modulators enabled by intraband transitions. *Nat. Commun.* **2012**, *3*, 780.
(19) Jessop, D. S.; Kindness, S. J.; Xiao, L.; Braeuninger-Weimer, P.; Lin, H.; Ren, Y.; Ren, C. X.; Hofmann, S.; Zeitler, J. A.; Beere, H. E.; Ritchie, D. A.; Degl'Innocenti, R. Graphene based plasmonic terahertz amplitude modulator operating above 100 MHz. *Appl. Phys. Lett.* **2016**, *108*, 17110.
(20) Degl'Innocenti, R.; Jessop, D. S.; Sol, C. W. O.; Xiao, L.; Kindness, S. J.; Lin, H.; Zeitler, J. A.; Braeuninger-Weimer, P.; Hofmann, S.; Ren, Y.; Kamboj, V. S.; Griffiths, J. P.; Beere, H. E.; Ritchie, D. A. Fast modulation of terahertz quantum cascade lasers using graphene loaded plasmonic antennas. *ACS Photonics* **2016**, *3*, 464−470.
(21) Degl'Innocenti, R.; Jessop, D. S.; Shah, Y. D.; Sibik, J.; Zeitler, A.; Kidambi, P. R.; Hofmann, S.; Beere, H. E.; Ritchie, D. A. Low-Bias Terahertz Amplitude Modulator Based on Split-Ring Resonators and Graphene. *ACS Nano* **2014**, *8*, 2548−2554.
(22) Docherty, C. J.; Lin, C.-T.; Joyce, H. J.; Nicholas, R. J.; Herz, L. M.; Li, L.-J.; Johnston, M. B. Extreme sensitivity of graphene photoconductivity to environmental gases. *Nat. Commun.* **2012**, *3*, 1228.
(23) Lemme, M. C.; Echtermeyer, T. J.; Baus, M.; Szafranek, B. N.; Bolten, J.; Schmidt, M.; Wahlbrink, T.; Kurz, H. Mobility in graphene double gate field effect transistors. *Solid-State Electron.* **2008**, *52*, 514−518.
(24) Worral, C. H.; Alton, J.; Houghton, M.; Barbieri, S.; Beere, H. E.; Ritchie, D. A. Continuous wave operation of a superlattic quantum cascade laser emitting at 2 THz. *Opt. Express* **2006**, *14*, 171−181.
(25) Xia, F.; Perebeinos, V.; Lin, Y.-M.; Yanqinq, W.; Avouris, P. The origins and limits of metal−graphene junction resistance. *Nat. Nanotechnol.* **2011**, *6*, 179−184.
(26) Khomyakov, P. A.; Starikov, A. A.; Brcks, G.; Kelly, P. J. Nonlinear screening of charges induced in graphene by metal contacts. *Phys. Rev. B: Condens. Matter Mater. Phys.* **2010**, *82*, 115437.
(27) Jadidi, M. M.; Sushikov, A. B.; Myers-Ward, R. L.; Boyd, A. K.; Daniels, K. M.; Gaskill, D. K.; Fuhrer, M. S.; Drew, H. D.; Murphy, T. E. Tunable Terahertz Hybrid Metal−Graphene Plasmons. *Nano Lett.* **2015**, *15*, 7099−7104.
(28) Siciliani de Cumis, U.; Xu, J. H.; Masini, L.; Degl'Innocenti, R.; Pingue, P.; Beltram, F.; Tredicucci, A.; Vitiello, M. S.; Benedetti, P. A.; Beere, H. E.; Ritchie, D. A. Terahertz confocal microscopy with a quantum cascade laser source. *Opt. Express* **2012**, *20*, 21924−21931.
(29) Sagade, A. A.; Neumaier, D.; Schall, D.; Otto, M.; Pesquera, A.; Centeno, A.; Elorza, A. Z.; Kurz, H. Highly air stable passivation of graphene based field effect devices. *Nanoscale* **2015**, *7*, 3558−3564.
(30) Zhou, Y.; E, Y.; Ren, Z.; Fan, H.; Xu, X.; Zheng, X.; Lei, D. Y.; Li, W.; Wang, L.; Bai, J. Solution-processable reduced graphene oxide films as broadband terahertz wave impedance matching layers. *J. Mater. Chem. C* **2015**, *3*, 2548−2556.
(31) Withers, F.; Hardistry Bointon, T.; Craciun, M. F.; Russo, S. All-Graphene Photodetectors. *ACS Nano* **2013**, *7*, 5052−5057.
(32) Kidambi, P. R.; Bayer, B. C.; Blume, R.; Wang, Z.-J.; Baehtz, C.; Weatherup, R. S.; Willinger, M.-G.; Schloegl, R.; Hofmann, S. Observing Graphene Grow: Catalyst−Graphene Interactions during Scalable Graphene Growth on Polycrystalline Copper. *Nano Lett.* **2013**, *13*, 4769−4778.
(33) Hofmann, S.; Braeuninger-Weimer, P.; Weatherup, R. S. CVD-Enabled Graphene Manufacture and Technology. *J. Phys. Chem. Lett.* **2015**, *6*, 2714−2721.
(34) Goykhman, I.; Sassi, U.; Desiatov, B.; Mazurski, N.; Milana, S.; de Fazio, D.; Eiden, A.; Khurgin, J.; Shappir, J.; Levy, Y.; Ferrari, A. C. On-Chip Integrated, Silicon−Graphene Plasmonic Schottky Photodetector with High Responsivity and Avalanche Photogain. *Nano Lett.* **2016**, *16*, 3005−3013.
(35) Mueller, T.; Xia, F.; Freitag, M.; Tsang, J.; Avouris, P. Role of contacts in graphene transistors: A scanning photocurrent study. *Phys. Rev. B: Condens. Matter Mater. Phys.* **2009**, *79*, 245430.

DOI: 10.1021/acsphotonics.6b00405
ACS Photonics 2016, 3, 1747−1753